Supporting information：

Characterization of Cl-doped two-dimensional $(PEA)_2PbBr_4$ perovskite single crystals for fast neutron and gamma ray detection

Wei Xie, Sha Gong, Fuyun Hu, Liping Peng *

Physics and Electronic Information College, Huanggang Normal University, Huanggang 438000, China

W Xie, Dr. S Gong, F Y Hu, Prof. L P Peng
Physics and Electronic Information College,

Huanggang Normal University,

Huanggang 438000, China

E-mail: pengliping@hgnu.edu.cn

1. X-ray detection performance of inorganic scintillator and organic scintillator and our materials

Table S1 X-ray detection performance of inorganic scintillator

Inorganic scintillator	Detectable ray	Photons MeV^{-1}	Luminescence Lifetime (ns)	References
$LaBr_3$: Ce	γ-ray	61 000	35	[1]
LYSO: Ce	γ-ray	32 000	40	[2]
CsI: Tl	γ-ray	54 000	1 220	[1]
NaI: Tl	γ-ray	41 000	230	[3]
$CdWO_4$	γ-ray	28 000	12 000	[4,5]
SrI_2: Eu	γ-ray	120 000	2 400	[6]
Cs_2LiYCl_6: Ce	γ-ray, thermal and fast neutron	20 000	50/1 000	[7]

Table S2 X-ray detection performance of organic scintillator

Organic scintillator	Detectable ray	Photons MeV^{-1}	Luminescence Lifetime (ns)	References
Anthracene	Fast neutron	20 000	30	[7]
Stillbene	Fast neutron	14 000	3.5-4.5	[7]
Zr-DPA @ PDMS	γ-ray	920	4.1	[8]
$CsPbBr_3$/I @ PMMA	γ-ray	9 000	30	[9]
$FAPbBr_3$ @ toluene	Fast neutron	1 282	NA	[10]
$(PEA)_2PbBr_4$	**Fast neutron**	**>30 000**	**10<**	**Our work**

2. Detection of crystal quality

In this experiment, the quality of the crystal was evaluated by means of transmittance, X-ray diffraction (XRD) and swing curve test.

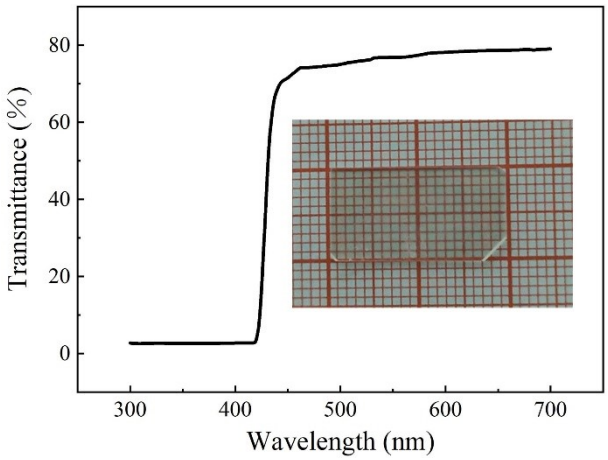

Figure S1. $(PEA)_2PbBr_4$ crystal transmittance curve, the illustration is a physical image of the obtained crystal.

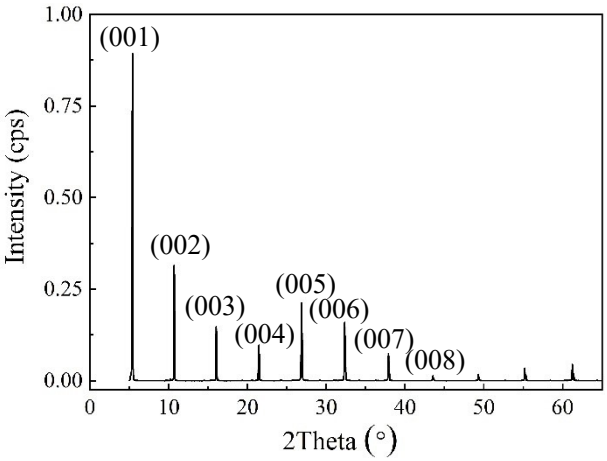

Figure S2. XRD results of $(PEA)_2PbBr_4$ crystal.

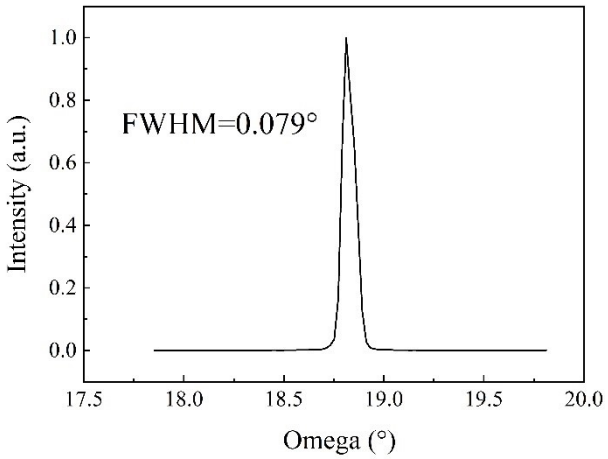

Figure S3. $(PEA)_2PbBr_4$ Results of swing curve test of single crystal with 2θ of 37.72°.

3. Absorption spectrum, PL spectrum and energy band curve

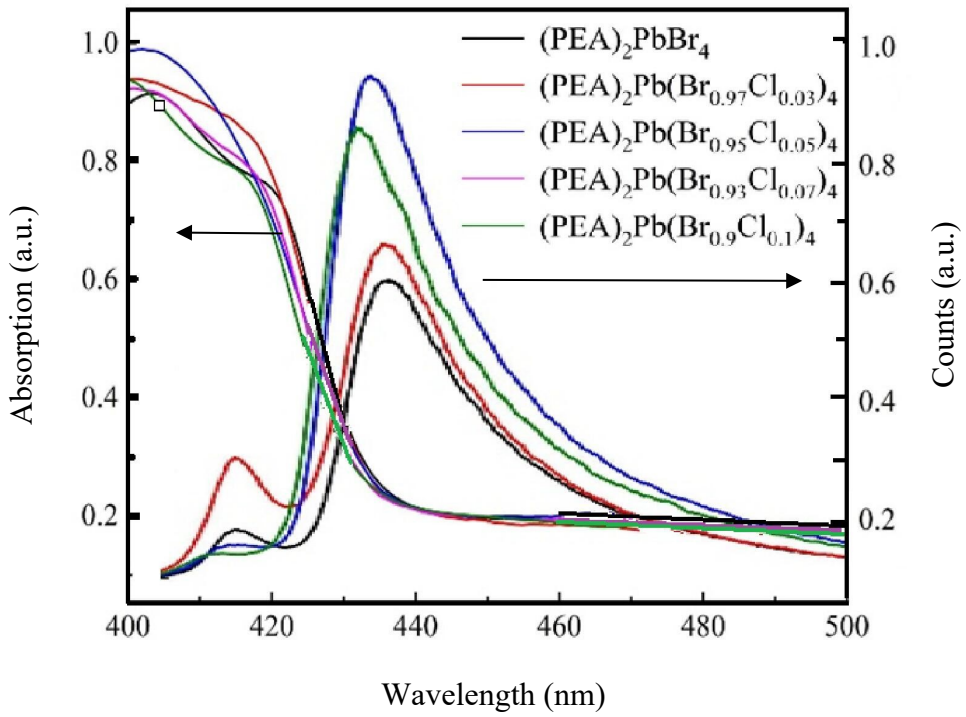

Figure S4. Cl^- doped $(PEA)_2PbBr_4$ of absorption spectrum and photoemission spectrum, (0, 3%, 5%, 10%, 17.5%, 100% doping concentration).

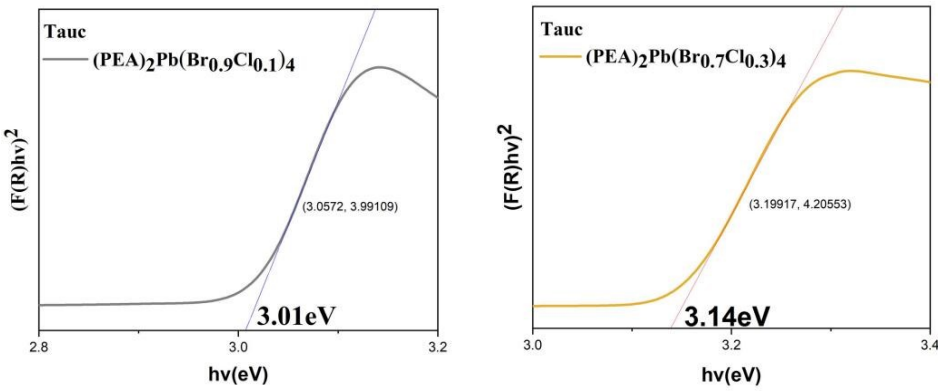

Figure S5. The fitting results of energy bands when different concentrations of Cl are doped (x=0.1, 0.3)

4. Source of neutrons

With deuterium-deuterium fusion reaction and deuterium-tritium fusion reaction as neutron sources, the nuclear reaction equations are shown in formula (1) and formula (2), and the released fast neutron energy is 2.45 MeV and 14.1 MeV respectively.

$$^{2}_{1}\mathrm{D} + ^{2}_{1}\mathrm{D} \xrightarrow{50\%} ^{3}_{2}\mathrm{He}\ (0.82\ \mathrm{MeV}) + ^{1}_{0}\mathrm{n}\ (2.45\ \mathrm{MeV}) \#(1)$$

$$^{2}_{1}\mathrm{D} + ^{3}_{1}\mathrm{T} \rightarrow ^{4}_{2}\mathrm{He}\ (3.5\ \mathrm{MeV}) + ^{1}_{0}\mathrm{n}\ (14.1\ \mathrm{MeV}) \#(2)$$

The D-D and D-T neutron tubes used are from Xi'an Guoneng Neutron Detection Technology Co., LTD. The neutron tube Model GN25. Figure S6 is a physical diagram of the device used for pulse amplitude spectrum test by D-T fusion reaction as a fast neutron source. The core components in the figure include high voltage, PMT and D-T neutron tube

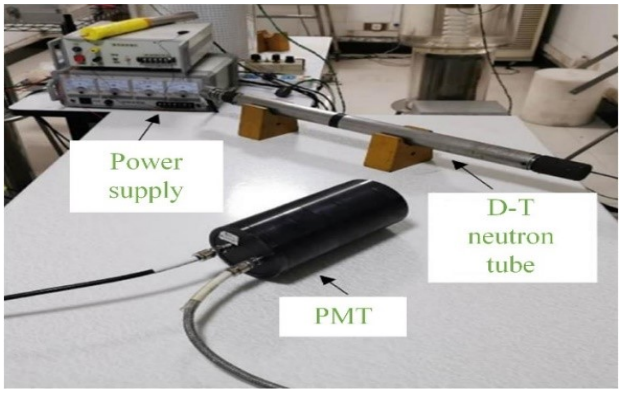

Figure S6.Test diagram of D-T fusion reaction as fast neutron source

In order to test the performance of two-dimensional halide perovskite in a mixed field containing fast neutrons and gamma rays, the Dense plasma focus (DPF) was used as a ray source. Since the 1980s, DPF devices have been used primarily as fusion teaching systems and neutron and gamma-ray sources.[11]

4. Working principle of dense plasma focus device and time-of-flight particle screening.

In order to test the performance of two-dimensional halide perovskite in a mixed field containing fast neutrons and gamma rays, the Dense plasma focus (DPF) was used as a ray source. As shown in Figure S5, the DPF was a compact device that uses a high current to ionize a deuterium gas, which is then compressed to produce a D-D fusion reaction, providing fast neutrons with an energy of 2.45 MeV and gamma rays with an energy of 67 KeV at an operating voltage of 16 to 20 KeV. The Photomultiplier tube (PMT) Model used in DPF mixed field detection is Hamamatsu, Model is H6410. The responses of $(PEA)_2Pb(Br_{0.95}Cl_{0.05})_4$ crystal and plastic scintillator EJ228 to the mixed field were recorded with two oscilloscopes, model number Tektronix TEK 4104B and Agilent Technologies DSO-X 4154A.

Figure S4 (b) illustrated the principle of Time of Flight (TOF) for particle identification. If we don't consider the relativistic effects, the time t_n required for fast neutrons to travel from the point of origin (where fusion occurs) to the detector can be obtained by the following formula:

$$t_n = \frac{L}{\sqrt{2E_n/m}} \#(1)$$

where L is the distance from the fusion point to the detector, E_n is the fast neutron energy, and m is the fast neutron static mass. Gamma photons are determined by the time required (t_γ) from the fusion point to the detector is determined by equation (2):

$$t_\gamma = \frac{L}{c} \#(2)$$

where c is the speed of light. Due to their different speeds, fast neutrons and gamma photons take different time to reach the detector after they are emitted from the same point source. At the same time, the time interval of the two nuclear fusion reactions can be judged by the difference in the time of the two fast neutrons arriving at the detector.

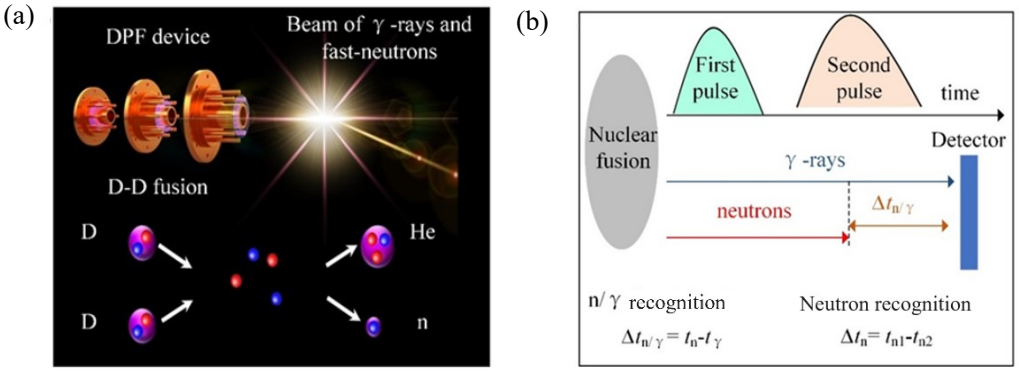

Figure S7. (a)Working principle of DPF device; (b) Principle of time-of-flight particle screening.

As shown in Figure. S8(a), compared with the background test results in the passive condition, the high channel part of the pulse amplitude spectrum in the D-D reaction or D-T reaction neutron source has an obvious flat rectangular counting region, which is because the energy transferred by fast neutrons is continuously distributed when they collide with hydrogen atoms. If the cutoff site is defined as the site corresponding to 1/2 of the maximum value in the declining edge of the rectangular curve, the cutoff site is 270 and 1645 respectively for the D-D reaction and D-T reaction neutron sources. The neutron emitted by the D-T reaction neutron source has a larger cutoff site because of its higher energy, and the cutoff site ratio (6.09) is close to the neutron energy ratio (5.76)

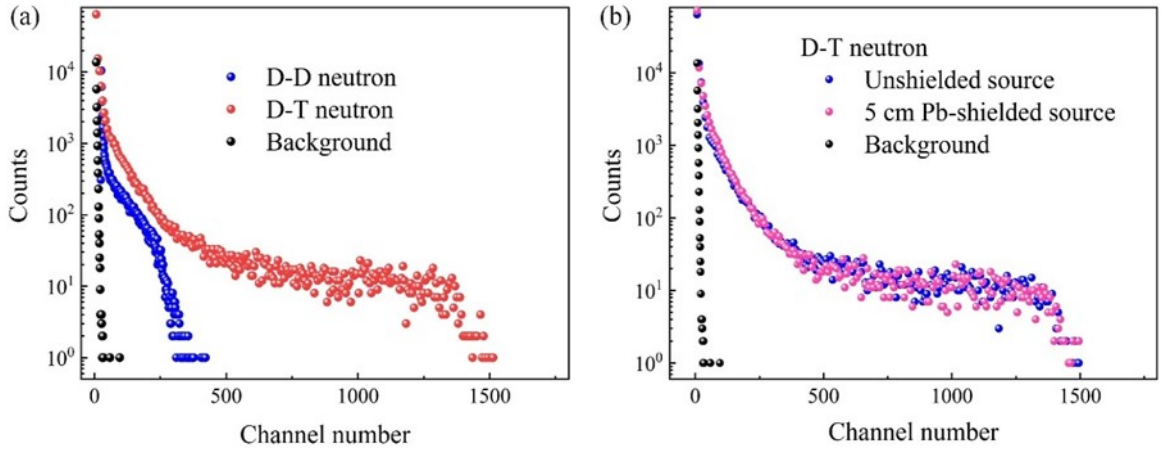

Figure S8 Neutron pulse amplitude spectrum: (a) Pulse amplitude spectrum test results when D-D fusion reaction and D-T fusion reaction are used as fast neutron sources; (b) Comparison of test results on whether the neutron source is shielded by Pb plate when the D-T fusion reaction is used as the neutron source

Further, in order to exclude the influence of the accompanying gamma rays in the D-T reaction on the test, the D-T neutron source is shielded by a 5 cm thick Pb plate. The test results are shown in Figure S8(b). The test results of pulse amplitude spectrum show that shielding or not has no obvious influence on the test results. In other words, the high track count in the pulse amplitude spectrum is mainly contributed by the interaction of fast neutrons with $(PEA)_2Pb(Br_{0.95}Cl_{0.05})_4$ crystals.

Reference:

[1] P. Lecoq. Development of new scintillators for medical applications. Nuclear Instruments and Methods in Physics Research Section A: Accelerators, Spectrometers, Detectors and Associated Equipment, 2016, 809: 130-139.

[2] I. Mouhti, A. Elanique, M. Y. Messous, A. Benahmed, J. E. McFee, Y. Elgoub, et al. Characterization of CsI(Tl) and LYSO(Ce) scintillator detectors by measurements and Monte Carlo simulations. Applied Radiation and Isotopes, 2019, 154: 108878.

[3] C. W. van Eijk. Inorganic scintillators in medical imaging. Physics in Medicine & Biology, 2002, 47(8): R85-R106.

[4] C. Michail, V. Koukou, N. Martini, G. Saatsakis, N. Kalyvas, A. Bakas, et al. Luminescence efficiency of cadmium tungstate ($CdWO_4$) single crystal for medical imaging applications. Crystals, 2020, 10(6): 429.

[5] S. P. Burachas, F. Danevich, A. S. Georgadze, H. Klapdor-Kleingrothaus, V. Kobychev, B. Kropivyansky, et al. Large volume $CdWO_4$ crystal scintillators. Nuclear Instruments and Methods in Physics Research Section A: Accelerators, Spectrometers, Detectors and Associated Equipment, 1996, 369(1): 164-168.

[6] M. Takabe, A. Kishimoto, J. Kataoka, S. Sakuragi, Y. Yamasaki. Performance evaluation of newly developed SrI_2(Eu) scintillator. Nuclear Instruments and Methods in Physics Research Section A: Accelerators, Spectrometers, Detectors and Associated Equipment, 2016, 831: 260-264.

[7] M. J. Cieslak, K. A. A. Gamage, R. Glover. Critical review of scintillating crystals for neutron detection. Crystals, 2019, 9(9): 480.

[8] J. Perego, I. Villa, A. Pedrini, E. C. Padovani, R. Crapanzano, A. Vedda, et al. Composite fast scintillators based on high-Z fluorescent metal−organic framework nanocrystals. Nature Photonics, 2021, 15(5): 393-400.

[9] M. Gandini, I. Villa, M. Beretta, C. Gotti, M. Imran, F. Carulli, et al. Efficient, fast and reabsorption-free perovskite nanocrystal-based sensitized plastic scintillators. Nature Nanotechnology, 2020, 15(6): 462-468.

[10] K. M. McCall, K. Sakhatskyi, E. Lehmann, B. Walfort, A. S. Losko, F. Montanarella, et al. Fast neutron imaging with semiconductor nanocrystal scintillators. ACS Nano, 2020, 14(11): 14686-14697.

[11] A. Link, C. Halvorson, E. C. Hagen, D. V. Rose, D. R. Welch, A. Schmidt. Particle-in-cell modeling for MJ scale dense plasma focus with varied anode shape. in: 9th International Conference on Dense Z Pinches. Napa, CA, USA, 3-6 Aug. 2014, Proceedings of the AIP, 2014: 23-26.